The formation and fate of internal waves in the South China Sea

Matthew H. Alford[1], Thomas Peacock[2], Jennifer A. MacKinnon[1], Jonathan D. Nash[3], Maarten C. Buijsman[4], Luca R. Centuroni[1], Shenn-Yu Chao[5], Ming-Huei Chang[6], David M. Farmer[7], Oliver B. Fringer[8], Ke-Hsien Fu[9], Pat Gallacher[10], Hans C. Graber[11], Karl R. Helfrich[12], Steven Jachec[13], Chris Jackson[14], Jody M. Klymak[15], Dong S. Ko[10], Sen Jan[6], T. M. Shaun Johnston[1], Sonya Legg[16], I-Huan Lee[9], Ren-Chieh Lien[17], Matthieu J. Mercier[18], James N. Moum[3], Ruth Musgrave[1], Jae-Hun Park[20], Andrew I. Pickering[17], Robert Pinkel[1], Luc Rainville[17], Steven R. Ramp[21], Daniel L. Rudnick[1], Sutanu Sarkar[22], Alberto Scotti[23], Harper L. Simmons[24], Louis C. St. Laurent[12], Karan Venayagamoorthy[25], Yu-Huai Wang[9], Joe Wang[6], Yiing J. Yang[6], Theresa Paluszkiewicz[19], Tswen-Yung (David) Tang[6]

[1]*Scripps Institution of Oceanography, University of California San Diego, La Jolla, CA 92037, USA*

[2]*Massachusetts Institute of Technology, Cambridge, MA, USA*

[3]*Oregon State University, Corvallis, OR, USA*

[4]*University of Southern Mississippi, Stennis Space Center, MS 39529, USA*

[5]*University of Maryland, Cambridge, MD 21613 USA*

[6]*Institute of Oceanography, National Taiwan University, Taipei, Taiwan*

[7]*University of Rhode Island, RI 02882, USA*

[8]*Stanford University, Stanford, CA 94305, USA*

[9]*National Sun-Yat Sen University, Kaohsiung, Taiwan*

[10]*Naval Research Laboratories, Stennis Space Center, MS 39529, USA*

[11]*University of Miami, Miami, FL 33149, USA*

[12]*Woods Hole Oceanographic Institution, Falmouth, MA 02543, USA*

[13]*Florida Institute of Technology, Melbourne, FL 32901, USA*

[14]*Global Ocean Associates, Alexandria, VA 22310, USA*

[15]*University of Victoria, Victoria, BC V8W 3P6, Canada*

[16]*Princeton University, NJ 08542, USA*

[17]*University of Washington, Seattle, WA, USA*

[18]*Institut de Mécanique des Fluides de Toulouse, Toulouse, France*

[19]*Office of Naval Research, Arlington, VA, USA*

[20]*Korea Institute of Ocean Science and Technology, Ansan, Korea*

[21]*Soliton Ocean Services, Carmel, CA 93924, USA*

[22]*University of California San Diego, La Jolla, CA 92037, USA*

[23]*University of North Carolina, Chapel Hill, NC 25599, USA*

[24]*University of Alaska at Fairbanks, Fairbanks, AK 99775, USA*

[25]*Colorado State University, Fort Collins, CO 80523, USA*

Internal gravity waves, the subsurface analogue of the familiar surface gravity waves that break on beaches, are ubiquitous in the ocean. Because of their strong

vertical and horizontal currents, and the turbulent mixing caused by their breaking, they impact a panoply of ocean processes, such as the supply of nutrients for photosynthesis[1], sediment and pollutant transport[2] and acoustic transmission[3]; they also pose hazards for manmade structures in the ocean[4]. Generated primarily by the wind and the tides, internal waves can travel thousands of kilometres from their sources before breaking[5], posing severe challenges for their observation and their inclusion in numerical climate models, which are sensitive to their effects[6-7]. Over a decade of studies[8-11] have targeted the South China Sea, where the oceans' most powerful internal waves are generated in the Luzon Strait and steepen dramatically as they propagate west. Confusion has persisted regarding their generation mechanism, variability and energy budget, however, due to the lack of *in-situ* data from the Luzon Strait, where extreme flow conditions make measurements challenging. Here we employ new observations and numerical models to (i) show that the waves begin as sinusoidal disturbances rather than from sharp hydraulic phenomena, (ii) reveal the existence of >200-m-high breaking internal waves in the generation region that give rise to turbulence levels >10,000 times that in the open ocean, (iii) determine that the Kuroshio western boundary current significantly refracts the internal wave field emanating from the Luzon Strait, and (iv) demonstrate a factor-of-two agreement between modelled and observed energy fluxes that enables the first observationally-supported energy budget of the region. Together, these findings give a cradle-to-grave picture of internal waves on a basin scale, which will support further improvements of their representation in numerical climate predictions.

Internal gravity waves are propagating disturbances of the ocean's density stratification. Their physics resembles that of surface gravity waves but with buoyancy rather than gravity providing their restoring force – making them much larger (10's to 100's of meters instead of 1 to 10 meters) and slower (hours instead of seconds). Generated primarily by tidal flow past seafloor topography and winds blowing on the sea surface, and typically having multi-kilometer-scale horizontal wavelengths, their estimated 1 TW of deep-sea dissipation is understood to play a crucial role in the ocean's global redistribution of heat and momentum[12]. A major challenge is to improve understanding of internal wave generation, propagation, steepening and dissipation, so that the role of internal waves can be more accurately incorporated in climate models.

The internal waves that originate from the Luzon Strait on the eastern margin of the South China Sea (SCS) are the largest documented in the global oceans (Figure 1). As the waves propagate west from the Luzon Strait they steepen dramatically (Figure 1a), producing distinctive solitary wave fronts evident in sun glint and synthetic aperture radar (SAR) images from satellites (Figure 1b). When they shoal onto the continental slope to the west, the downward displacement of the ocean's layers associated with these solitary waves can exceed 250 m in 5 minutes[8]. On such a scale, these waves pose hazards for underwater navigation and offshore drilling[4], and supply nutrients from the deep ocean that nourish coral reefs[1] and pilot whale populations that forage in their wakes[13].

Over the past decade a number of field studies have been conducted in the region; this work has been comprehensively reviewed[10,11]. All of these studies, however, focused on the propagation of the internal waves across the SCS and their interactions with the continental shelf of China. Until the present study there had been no substantial *in situ* data gathered at the generation site of the Luzon Strait, in large part because of the extremely challenging operating conditions. A consequence has been persistent

confusion regarding the nature of the generation mechanism[11]; an underlying cause being the sensitivity of the models employed to the system parameters, such as the chosen transect for a two-dimensional model, the linear internal wave speed or the assumed location of the waves' origin within the Luzon Strait. Furthermore, the lack of *in situ* data from the Luzon Strait has meant an inability to test numerical predictions of energy budgets[9] and no knowledge of the impact of the Kuroshio on the emergence of internal solitary waves[11].

The goal of IWISE is to obtain the first comprehensive *in situ* data set from the Luzon Strait, which in combination with high-resolution three-dimensional numerical modeling supports a cradle-to-grave picture of the life cycle of the world's largest oceanic internal waves (see Methods section for extensive details). IWISE is the most substantial internal wave field program since the Hawaiian Ocean Mixing Experiment (HOME) revealed how most of the tidal losses from a complex ocean ridge system can be radiated away as nearly-sinusoidal waves, with a small fraction dissipated locally[14]. IWISE is significantly broader in scope, however, as the radiated internal tide is nonlinear and therefore subject to additional steepening and wave breaking processes. A pilot study was performed in the summer of 2010 to determine the feasibility of operating at desired locations[15], and the full field program was executed throughout the summer of 2011. This Letter is a synthesis of the results from both programs.

The internal tides derive their energy from the barotropic (i.e. surface) tide, the flow arising from astronomical forcing of the oceans by the sun and the moon. The barotropic tides in this region are a combination of twice-daily (semidiurnal, D2) and once-daily (diurnal, D1) motions, giving rise to a strong diurnal inequality and a fortnightly amplitude envelope due to the interaction of lunar and solar tides (Figure 1d). Our moorings, shipboard stations, and autonomous gliders within and to the west of the Luzon Strait reveal time-averaged westward energy fluxes of 40±8 kWm^{-1} (Figure

2a; see Methods). Such values are about 100 times typical open-ocean values[16] and exceed any other known generation site around the world[15]. Measured fluxes agree to within a factor of two in magnitude and ±30° in direction with predictions of our far-field numerical model (see Methods), as well as previous numerical predictions[9].

Total energy flux in the northern section of the Luzon Strait shows a clockwise pattern between the tall east and west ridges (Figure 2a). This feature exists because the double-ridge structure creates a 100km-scale resonant cavity for the ~100km wavelength semi-diurnal internal tide[17], and is further confirmed by observations of very high energy density but little energy flux between the two ridges that is characteristic of a standing wave pattern[15]. Tidal flow transiting the ridge in the vicinity of the Batanes Islands (Figure 2f) gives rise to dramatic localized lee wave phenomena[18]. Shipboard time series of velocity and density, obtained at the location of the dashed lines in Figures 2b and 2c, are presented in Figure 2d. Observed vertical displacements of the ocean layers reach up to 500m, with static instabilities >200 m high. The associated depth-integrated turbulent dissipation levels (Figure 2e; see Methods) approach 20 Wm^{-2}, exceeding open ocean values by a factor of 1,000-10,000[8,11]. The associated vertical mixing of quantities such as temperature and salinity is sufficiently high ($>10^{-1}$ m s^{-1}), again orders of magnitude greater than open ocean values, that it likely plays a key role in setting large-scale circulation patterns throughout the South China Sea[19].

There was no evidence of significant nonlinear internal waves east of 120.5°E, finally laying to rest a widely stated conjecture that the large-amplitude internal solitary waves arise in the immediate vicinity of the Luzon Strait via a hydraulic lee wave mechanism[11]. Rather, what emerges immediately to the west of the Luzon Strait is a broad, energetic and spatially-coherent, nearly sinusoidal internal tide (Figure 1a, 2a and 3a,b) at a combination of semidiurnal and diurnal frequencies (Figure 1d). The structure

of the wave field is dominated by so-called mode-1 behavior[15], this being the fundamental vertical mode of oscillation in which velocity in the upper few hundred meters of the ocean is in the opposite direction to, and oscillates out of phase with, that in the deeper ocean (Figure 3c). The three-dimensional structure of the ridge system within the Luzon Strait shapes the radiated semidiurnal and diurnal internal tides differently because the horizontal wavelength of the former is half that of the latter. Semi-diurnal internal tide energy flux is strongest within a beam that emanates from the central section of the Luzon Strait, between 20^{o}-21^{o}N (Figure 3a), while a broader beam of diurnal energy flux emanates from across the central and southern sections of the Luzon Strait. These beams are also evident in the field data: characteristic diurnal energy fluxes of ~5 kW m^{-1} and ~20 kW m^{-1} were detected in the central and southern sections of the Luzon Strait, respectively; corresponding values for the semi-diurnal energy fluxes were ~20 kW m^{-1} and ~10 kW m^{-1} [15]. These results and interpretations were furthermore supported by a rotating, large-scale laboratory experiment, using an accurate scale model of the Luzon Strait[20].

The combination of mode-1 dominated semidiurnal and diurnal internal tides sets the initial condition for the evolution of large-amplitude solitary waves[20]. Whether or not steepening occurs depends crucially on the balance between nonlinearity and rotational dispersion, which serve to enhance and reduce the steepness of the wavefronts, respectively[22,23]. When the semidiurnal internal tide dominates, nonlinearity can overcome rotational dispersion leading to the formation of internal solitary waves around 120^{o}E as seen in Figure 1a,b; if diurnal forcing dominates, however, rotational dispersion tends to suppress formation. Other factors are the fortnightly spring-neap cycle (Figure 1d), which sets the overall amplitude of barotropic tidal forcing in the Luzon Strait, and the interaction between the semidiurnal and diurnal tides, which can cause alternating strong and weak wave fronts[21].

Another key influence on the radiated waves is the Kuroshio, one of the oceans' foremost boundary currents, whose modeled lateral structure and velocities of over 0.5 m s^{-1} were for the first time confirmed by our measurements (Figure 4a). The Kuroshio refracts the internal tide when it intrudes into the Luzon Strait, such that its location profoundly affects the subsequent propagation path of the waves. For example, we determine that the orientation of the semidiurnal beam was notably different during our winter 2010-2011 field study compared to a previous field study in winter 2006[24], for which moorings were deployed near Dongsha Island[25]. As no solitary waves were detected in winter by the latter study (Figure 4b), a conclusion was drawn that solitary waves are not present in the South China Sea during the wintertime. This is not the case, however, as solitary waves persisted throughout the winter of our 2010-2011 field study (Figure 4c)[24]. Rather, we determine that during winter 2006 the Kuroshio was responsible for directing the semidiurnal internal tide beam, and thus the solitary waves, south of the mooring location[24].

Proceeding into the shallower waters of the Dongsha Plateau at speeds of roughly 3 m s^{-1}, the internal solitary waves begin to slow down[26]. Eventually, the wave-induced fluid velocities can exceed the wave speed leading to the formation of trapped cores[27], wherein fluid is carried along with the wave. At this stage, the waves vertically displace water up to 170 m, nearly 40% of the local ocean depth, in only a few minutes and have wavelengths of only a few hundred meters. The solitary waves become highly turbulent, leading to strong vertical mixing that has been postulated to contribute to the high biological productivity in the vicinity of the nearby Dongsha coral atoll[1]. We observed the waves to become convectively and shear unstable, producing vertical overturns of up to one hundred meters within the core. Measured turbulent dissipation rates are extreme, exceeding 1.5×10^{-4} W kg^{-1}, contributing to a cross-shelf integrated dissipation level of 10 kW per meter of coastline.

The combination of IWISE numerical models and field measurements enables us to provide the first assessment of an energy budget for internal waves throughout the entire South China Sea, as summarized in Figure 3c. Our far-field model (see Methods) predicts that, out of a total conversion of 24 GW from the barotropic tide at the Luzon Strait, 15 GW are radiated to the east and west, agreeing to within a factor of two with observations; this suggests that around 40% of the energy is dissipated locally at the Luzon Strait. For comparison, our higher-resolution near-field model, which only captured the generation region, obtains a similarly high fraction of locally dissipated energy, but conversion and fluxes are about 1.8 times higher. These results suggest that the Luzon Strait is a more highly dissipative system than the Hawaiian Ridge[28], where only about 15% of the energy is dissipated locally. Differences between the two models, however, which we attribute to model resolution and their inability to directly resolve turbulence, emphasize that further computational advances are still required for quantitative certainty.

The observed westward energy flux at 120°E is approximately equipartitioned between semidiurnal and diurnal motions, with no energy yet in the sharp wavefronts. Closer to the continental slope at 117.25°E, however, the nonlinear internal waves (NLIW) gain energy at the expense of the internal tide, and energy is more equal among all three components (D1, D2 and NLIW). At the continental slope, the diurnal motions are partially reflected (eastward arrows at 117.895°E), while the steeper semidiurnal motions and nonlinear waves are transmitted, with active turbulence dissipating about 3 kW m^{-1} [29]. By 115.19°E, strong dissipation due to wave breaking over the continental shelf has removed nearly all energy in the nonlinear waves and internal tides.

The comprehensive modelling and measurements of the IWISE program have resulted in a first-order energy budget and an understanding of the key physical processes occurring in the Luzon Strait that lead to the formation of the world's

strongest internal waves. Conversion from the barotropic tide leads to strong internal tides accompanied by vigorous near field turbulence. These internal tides radiate westward through the strong Kuroshio currents, steepen into sharp wavefronts, and eventually break on the continental shelf. In spite of this clear physical picture, some questions remain including the precise fraction of energy dissipated locally and the role of the Kuroshio in modulating the wave amplitudes. Tackling challenges such as these, with a view toward improving representation of internal waves and their associated vertical mixing in numerical climate predictions, will require ever more sophisticated and highly-resolved numerical models that can successfully capture the weakly nonlinear, nonhydrostatic, and strongly nonlinear mechanisms[30].

References

1. Wang, Y. H., Dai, C. F. & Chen, Y. Y. Physical and ecological processes of internal waves on an isolated reef ecosystem in the South China Sea. *Geophys. Res. Lett.* 34 (2007).
2. Bogucki, D., Dickey, T. & Redekopp, L. Sediment resuspension and mixing by resonantly generated internal solitary waves. *J. Phys. Oceanogr*., 27(7), 1181–1196 (1997).
3. Williams, K. L., Henyey, F. S., Rouseff, D., Reynolds, S. A. & Ewart., T. Internal wave effects on high- frequency acoustic propagation to horizontal arrays-experiment and implications to imaging. *IEEE J. Oceanic Eng*., 26(1), 102–112 (2001).
4. Osborne, A. R., Burch, T. L. & Scarlet, R. I. The influence of internal waves on deep-water drilling. *J. Petroleum Tech*., 30(10), 1497–1504 (1978).
5. Ray, R. D. & Mitchum, G. T. Surface manifestation of internal tides generated near Hawaii. *Geophys. Res. Lett*., 23(16), 2101–2104 (1996).
6. Simmons, H., Jayne, S., Laurent, L. S. & Weaver, A. Tidally driven mixing in a numerical model of the ocean general circulation. *Ocean Model*., 82, 245–263, (2004).

7. Melet, A., Hallberg, R., Legg, S. & Polzin, K. L. Sensitivity of the ocean state to the vertical distribution of internal-tide-driven mixing. *J. Phys. Oceanogr.*, 43(3), 602–615 (2013).

8. Ramp, S. R. *et al.* Internal solitons in the northeastern South China Sea, part I: sources and deep-water propagation. *IEEE J. of Oceanic Engr.* 29, 1157–1181 (2004).

9. Jan, S., Lien, R. & Ting, C. Numerical study of baroclinic tides in Luzon Strait. *Journal of Oceanography* 64, 789–802 (2008).

10. Cai, S., Xie, J. & He, J. An overview of internal solitary waves in the South China Sea. *Surv. Geophys.* 33, 927–943 (2012).

11. Guo, C. & Chen, X. A review of internal solitary wave dynamics in the northern South China Sea. *Progress in Oceanography* 121, 7–23 (2014).

12. Ferrari, R. & Wunsch, C. Ocean circulation kinetic energy: Reservoirs, sources, and sinks. *Annual Review of Fluid Mechanics* 41, 253–282 (2009).

13. Moore, S. & Lien, R.-C. Pilot whales follow internal solitary waves in the South China Sea. *Marine Mammal Science* 23, 193–196 (2007).

14. Rudnick, D. *et al.* From tides to mixing along the Hawaiian Ridge. *Science* 301, 355–357 (2003).

15. Alford, M. H. *et al.* Energy flux and dissipation in Luzon Strait: Two tales of two ridges. *J. Phys. Oceanogr.* 41, 2211–2222 (2011).

16. Alford, M.H. Energy available for ocean mixing redistributed through long-range propagation of internal waves. *Nature* 423, 159–163 (2003).

17. Buijsman, M. *et al.* Three-Dimensional Double-Ridge Internal Tide Resonance in Luzon Strait. *J. Phys. Oceanogr.* 44, 850–869 (2014).

18. Pinkel, R., Buijsman, M. & Klymak, J. M. Breaking topographic lee waves in a tidal channel in Luzon Strait. *Oceanography* 25, 160–165 (2012).

19. Qu, T., Du, Y. & Sasaki, H. South China Sea throughflow: A heat and freshwater conveyor. *Geophys. Res. Lett*., 33, L23617 (2006).

20. Mercier, M., Gostiaux, L., Helfrich, K., Sommeria, J., Viboud, S., Didelle, H., Ghaemsaidi, S. J., Dauxois, T. & Peacock T. Large-scale realistic modeling of M2 internal tide generation at the Luzon Strait. *Geophys. Res. Lett*., 40, 5704-5708 (2013).

21. Li, Q. & Farmer, D. The generation and evolution of nonlinear internal waves in the deep basin of the South China Sea. *Journal of Physical Oceanography* 41, 1345–1363 (2011).

22. Helfrich, K. R. & Grimshaw, R. H. J. Nonlinear disintegration of the internal tide. *J. Phys. Oceanogr.* 38, 686–701 (2008).

23. Farmer, D., Li, Q. & Jae-Hun Park. Internal wave observations in the South China Sea: the role of rotation and nonlinearity. *Atmos.-Ocean.* 47, 267–280 (2009).

24. Park, J.-H. & Farmer, D. M. Effects of Kuroshio intrusions on nonlinear internal waves in the South China Sea during winter. *J. Geophys. Res.* 18, 7081–7094 (2013).

25. Ramp, S. R., Yang, Y. & Bahr, F. L. Characterizing the nonlinear internal wave climate in the Northeastern South China Sea. *Nonlin. Proc. Geophys.* 17, 481–498 (2010).

26. Alford, M.H. *et al.* Speed and evolution of nonlinear internal waves transiting the South China Sea. *J. Phys. Oceanogr.* 40, 1338–1355 (2010).

27. Lien, R.-C., Henyey, F., Ma, B. & Yang, Y.-J. Large-amplitude internal solitary waves observed in the northern South China Sea: Properties and energetics. *J. Phys. Oceanogr.* 44, 1095–1115 (2014).

28. Klymak, J. M. *et al.* An estimate of tidal energy lost to turbulence at the Hawaiian Ridge. *J. Phys. Oceanogr.* 36, 1148–1164 (2006).

29. Klymak, J.M., Alford, M.H., Pinkel, R. ,Lien, R.C. & Yang, Y.J. The breaking and scattering of the internal tide on a continental slope. *J. Phys. Oceanogr.* 41, 926–945 (2011).

30. Vitousek, S. & Fringer, O. B. Physical vs. numerical dispersion in nonhydrostatic ocean modeling. *Ocean Modelling* 40, 72–86 (2011).

Supplementary Information

Acknowledgements

This article is dedicated to T-Y Tang. Our work was supported by the U.S. Office of Naval Research and the Taiwan National Science Council. We are indebted to the Captains and crew of all of the research vessels that supported this work, as well as to the technical staff of the seagoing institutions. Without the skill and hard work of all of these people, these observations would not have been possible.

Author Contributions

All authors contributed to the paper in multiple ways. Primary writing: MHA, TP, JAM, JDN. Synthesis, overall coordination: Th.P, TYT. Energy flux calculations: MHA, AIP. Energy budget calculation: MHA, MCB, MC, RCL, JMK, LCS. Near-field moorings and calculations: MHA, AIP, LR, JDN, JNM, MHC. Far-field moorings and calculations: LRC, MHC, RCL, SR, YJY,TYT. Near-field CTD measurements (Figure 2d): RP, RM. Near-field LADCP measurements: MHA, JDN, JAM, LR, HLS,

AIP. Pressure inverted Echo Sounder (PIES) measurements: DMF, JHP, YJY, MHA. Microstructure measurements: LCS, KHF, HLS, YHW. Remote sensing: CJ, HCG. Theory: KRH, DF. Glider measurements: TMSJ, DLR. Regional contextualization, logistical support: S-YC, I-HL, SR, JW, YJT, TYT. Far-field modeling: SJ, HLS. 2D modeling: JMK, SS, AS, RM, KV. Near-field modeling: MCB, OBF, SL, SJ. Kuroshio modeling: PG, SJ, DSK. Laboratory measurements: TP, MJM.

Author Information

The authors declare that they have no competing financial interests.

Correspondence and requests for materials should be addressed to Matthew Alford (email: malford@ucsd.edu).

Figure Legends

Figure 1. Overview of internal waves in the South China Sea. (a) Vertical displacement of ocean layers near 200 m depth from the far-field numerical simulation. (b) A collage of Synthetic Aperture Radar (SAR) images taken on 12 August 2009, 04 August 2009 and 25 April 2005. Wave fronts are visible because they focus surface waves, increasing sea surface roughness. (c) Instrumentation deployed during IWISE. The Kuroshio is sketched schematically. (d) Time series of depth-averaged tidal current in Luzon Strait over a spring/neap cycle, showing the presence of once-daily (diurnal, D1) and twice-daily (semidiurnal, D2) frequencies.

Figure 2. Near-field processes in the Luzon Strait. (a) Time-mean total energy flux from the near-field numerical model (white arrows) and field measurements (colored arrows). (b,c) Snapshots from the 2D model showing internal wave breaking at the location indicated in (a), corresponding to times T_0 and T_1 indicated in figure (f). Colors and lines in (b) and (c) indicate east-west velocity and density contours, respectively. (d) Corresponding field measurements at the location of the vertical dashed line in (b,c). (e) Depth-averaged dissipation rate computed from Thorpe scales. (f) Depth-integrated eastward tidal transport, showing the times T_0, T_1 of the frames in (b,c).

Figure 3. Internal wave energy fluxes in the South China Sea. (a) Semidiurnal and (b) diurnal energy flux from the far-field model. (c) Energy flux and (d) bathymetry along 21^oN. The processes of generation, breaking, propagation, steepening and dissipation are shown schematically. Arrows in (c) indicate energy fluxes at 21^oN in the semidiurnal and diurnal internal tides and in the solitary or nonlinear internal waves

(NLIW). Flux values at 120°E are from the near-field model; flux and dissipation values at 115.19°E, 117.25°E and 117.895°E are from observations (see Methods).

Figure 4. The Kuroshio and its impact on wave propagation. (a) Observed (green) and modeled (gray) Kuroshio flow during June-August 2011 in the Luzon Strait region. The meshes are modeled phase lines of internal waves during Feb 2006 (red) and Feb 2011 (blue). (b,c) Measured wave displacement at the locations shown in (a). Waves were observed year-round at the southern station in 2011 (c), but not at the northern station in 2006 (b), when the Kuroshio deflected the internal wave paths southward (a, red).

Methods

Numerical models

Several numerical models were used in this paper, representing varying degrees of resolution, domain size and resolved processes. Four 3D models with realistic bathymetry and stratification were employed, namely a "far-field" model, a "near-field" model, and two "Kuroshio" models. A 2D (horizontal-vertical) model was also employed.

The 3D models were used to simulate basin-scale waves, near-field physical processes, and the role of the Kuroshio, respectively. All were forced with predictions using 8 tidal constituents (K1, O1, P1, Q1, K2, M2, N2 and S2) from a barotropic tidal model, TPXO7.2[31] which was validated against measured currents in the region in this and a previous experiment[15,25]. Bathymetry was from multibeam depth soundings where available, and from the 30 arc-second database[32] elsewhere. Stratification was horizontally uniform in the far-field and near-field models, obtained from the generalized digital environmental model database (GDEM) climatology for the month

of August[33] for the far-field model and from August 2010 field data for the near-field model. Stratification in the Kuroshio models was from larger-scale data-assimilating regional simulations.

The far-field model (Figures 1(a), 3(a) and 3(b)) is based on the Hallberg isopycnal model[34] and encompasses the entire South China Sea with a spatial resolution of 2km and 40 layers in the vertical[35]. The near-field model data (Figure 2a), with a horizontal resolution of 250m, were generated using a 154-layer implementation of the MITgcm, based on the configuration in ref. 10. The MITgcm[36] was also used to generate the two-dimensional numerical results presented in figures 2(b) and 2(c). For this, the bathymetry was a transect taken from the near-field model and calculations were performed using a telescoped grid with horizontal and vertical resolutions of 7.8m and 6.1m, respectively. None of the models explicitly resolve the 3D turbulence that is directly responsible for model energy dissipation.

The two Kuroshio models used are different implementations, but similar in their resolution, intent and skill. One (Figure 4a, vectors) is an application of the NRL Ocean Nowcast/Forecast[37-39], an integration of the Navy Coastal Ocean Model (NCOM) and a statistical data-analysis model. In addition to the tidal forcing, the model's open boundary conditions are from a larger scale model for the entire East Asian seas[40]. The second model, used to generate the ray paths (Figure 4c, red/blue meshes), is a data-assimilating version of the Hybrid Coordinate Ocean Model (HYCOM)[41].

Shipboard measurements

The basic physical quantities required to characterize physical ocean flows are the potential density (density with the compression effects of hydrostatic pressure removed) and velocity. The former is measured with CTDs (conductivity temperature depth

instruments) that are repeatedly lowered and raised from a shipboard winch. Salinity (S) is computed from temperature (T), conductivity and pressure (P) measurements, and density is then a function of salinity, temperature and pressure. Velocity is measured with ADCPs (acoustic Doppler current profilers). Affixed to the hull of the ship or lowered with the CTD instrument, velocity is measured as a function of depth beneath the ship by the phase shift of 75-KHz acoustic pulses backscattered from the water column. The precision of CTD and ADCP measurements depends on set-up and several other factors. Typical uncertainties for density and velocity are 2×10^{-4} kg m^{-3} and 0.01 m s^{-1}, respectively, which are one to two orders of magnitude less than the signals described here. The energy flux measurements presented in Figure 2a (flux calculation described next) are computed from 36-hour stations wherein velocity and pressure are repeatedly measured by cycling the CTD up and down approximately once each hour. The measurements in Figure 2e are from a specialized "fast CTD" system[18] designed to sample much faster than a conventional CTD (a profile every approximately ten minutes as opposed to about an hour, depending on water depth).

Glider measurements

The first measurements of energy flux were made from autonomous gliders[42] as part of IWISE (Figure 1c). Gliders are autonomous underwater vehicles that move up and down through the water by adjusting their buoyancy, which is accomplished by filling and draining oil from a bladder. Wings allow the glider to "fly" through the water at about 0.25 m s^{-1}. During IWISE, two gliders were deployed for about two months each, and sampled density and velocity in the upper 500 m each 3 hours.

Moored measurements

Three types of moored measurements were made during IWISE. *Profiling moorings* featuring a McLane Moored Profiler[43] (MP) crawling up and down a vertical moored wire approximately each 1.5 hour between 300-400 m below the surface and about 10 m above the bottom. Above, a series of approximately 30 densely-spaced temperature loggers and an ADCP gave temperature (from which density was computed) and velocity in the upper ocean. The MPs carried current meters and CTDs, giving continuous, full-water-column measurements of density and velocity from a mooring, a challenging task.

ADCP/T-chain moorings had only ADCPs and temperature and/or salinity measurements, giving faster sampling at the cost of continuous data. Both of these types of moorings were prone to significant knockdowns by the extreme currents in Luzon Strait. Knockdowns were minimized by highly taut designs and (for one mooring) a low-drag cylindrical float. When they occurred (up to 100 m in the worst case), they were corrected for by means of pressure measurements on the top subsurface floats.

A final moored measurement was bottom-mounted *Pressure Inverted Echo Sounders (PIES)*, which measure bottom pressure and the round-trip bottom-top-bottom travel time of an acoustic pulse transmitted upward every few seconds. Since sound speed depends on temperature, these signals are proportional to the mode-1 displacement of the thermocline[44]. True mode-1 displacements in Figures 4(a) and (b) were computed from travel time using nearby moored in-situ temperature measurements, and have an overall uncertainty of 4 m[33].

Turbulence measurements

The turbulence measurements described on the continental shelf were obtained directly using a Vertical Microstructure Profiler (VMP). The turbulent dissipation rate, ε, was estimated by fitting small-scale velocity shear observations to a theoretical spectrum and integrating following ref. 45. The turbulent dissipation results in Figure 2 were obtained indirectly using the method of overturns or "Thorpe sorting"[46], which computes the outer scale of the turbulence via the vertical distance parcels of water have moved from a stably stratified profile. Numerous previous studies[46-48] have demonstrated good agreement with direct measurements; although recent modeling work[49] has given rise to the possibility that Thorpe-based estimates could be biased high by a factor as great as 2-6.

Synthetic Aperture Radar (SAR) imagery

Although nonlinear internal waves propagate in the interior of the ocean, their currents produce convergent (rough) and divergent (smooth) zones on the ocean surface that move in phase with their subsurface crests and troughs. These variations in surface roughness create the distinctive light/dark pattern of the internal wave packets found in synthetic aperture radar images of the ocean (Figure 1b), which have typical horizontal resolution of tens of meters. The technique is sensitive to the background roughness of the sea surface, which depends on wind speed and other factors. Therefore, imagery is an excellent indicator of the location and morphology of the wave fronts, but generally cannot give wave amplitude.

Energy flux

Internal tide energy flux (presented in Figures 2(a) and 3) is computed from both model and observed data as the depth integral of $\langle \mathbf{u}' p' \rangle$, where $\mathbf{u}'$ is the measured

velocity fluctuation with the barotropic tide removed and p' is the baroclinic pressure, computed from density assuming hydrostatic balance[50].

Energy flux is computed separately for the semidiurnal and diurnal motions by use of harmonic analysis. Shipboard stations are always ≥36 hours, allowing separation of these motions from each other and from the inertial frequency, which is 33.4 hours at this latitude. For each 36-hour station or 3-day time period in the case of moored and glider data, least-square fits are done at each depth to semidiurnal, diurnal and inertial motions. Much longer time series (~14 days) would be required to separate the different tidal constituents within each band (e.g. M2/S2 and K1/O1), so the diurnal and semidiurnal motions are referred to as D1 and D2, respectively.

Nonlinear coupling between different frequencies would complicate our method of separation into bands. To ensure that nonlinear terms are not important in this context, the sum of the separated fluxes is compared to the total flux prior to separation. The two agree to within 10%[15,17,51].

Because it requires a vertical integral, the calculation of p' relies on full-water-column data. Therefore, gaps in the water column measurements give rise to errors, particularly when they are near the surface where the flux is the greatest. For the model data and CTD/ADCP station measurements (Figure 2a) gaps and associated errors are negligible. For the moored measurements where gaps are only tens of meters out of thousands, the associated errors are about 20%[51,52], which are determined by sampling the full-water-column model output with the coverage of the moorings. For the glider measurements, which sample only the upper 500 m, calculation of energy flux relies on fitting the data to the first baroclinic mode. Although the moored data verify that the bulk of the energy is in this mode, glider uncertainty in total flux is ≈30%[53].

To account for modulation by the spring/neap cycle, flux values from 36-h stations are converted to time-mean values by scaling them with the square of the barotropic velocity during the time of observations[15]. Values from moorings, which directly measure this modulation, are simply the time-mean for each constituent.

Energy flux of nonlinear waves (presented in Figure 3) has two additional terms in addition to the linear term computed above for the internal tides. An accurate expression for the energy flux of nonlinear waves is cE, where c is the wave speed and E is the sum of their kinetic and available potential energy[54]. The nonlinear waves' short timescales (minutes as opposed to hours for the internal tides) enables them to be easily isolated from the internal tides by means of bandpass filtering.

Energy Budget Calculation

While in general internal wave energy arises from a combination of wind and tidal forcing, in Luzon Strait the dominant energy source is the barotropic tide. Conversion to from barotropic tidal motions to baroclinic energy can be quantified as $C = U_{BT} \cdot \nabla Hp_{bot}$. Though observations can be used to compute conversion[55], they are far too sparse to estimate the integral over the near field region, so we use the model (uncertainties presented below).

In steady state, an energy budget for the internal tides (which here we consider to be comprised of only the nearly-sinusoidal waves) can be written as

$$C - \nabla \cdot F = D, \qquad (1)$$

where D represents all processes removing energy from the internal tide including dissipation and transfer of energy to the sharp nonlinear waves seen to the west. In the near-field region where no nonlinear waves are yet present, D represents primarily

turbulent processes. In the west, reductions in internal tide flux also arise as nonlinear wave fluxes increase (Figure 3).

None of the models resolve turbulence. However, the 2D and 3D near-field models resolve the processes that lead to it, primarily breaking lee waves as shown in Figure 2. Dissipation in these models is computed from a closure scheme[56] similar to the above Thorpe sorting algorithm used in the measurements. Observed and measured dissipation have been demonstrated to be within a factor of two of one another in breaking lee waves observed at several sites in the Luzon Strait[17] and one at the Hawaiian Ridge[57], but a detailed comparison at Luzon Strait is not yet complete.

The integrated conversion and fluxes discussed in the main text are computed by integrating the far-field model (Figure 3a,b) over the domain (19°-20.5°N, 120°-122.5°E). Flux and dissipation values plotted in Figure 3c are all from measurements near 21°N[29,58,59]. Measurements along a line rather than integrated values are subject to reduction by cylindrical spreading. As evident in Figure 3a,b, the model shows a factor-of-two reduction in fluxes along 21°N for D1, with <20% reduction for D2 owing to differences in their generation geometry.

Measurements at 120E are from gliders, which agree well with the far-field model[53]. Internal tide and nonlinear internal wave flux estimates further to the west are from moorings. Turbulence estimates on the continental slope and upper shelf are from Thorpe scales, while those west of 117.25°E are directly measured with the VMP. The separate eastward and westward fluxes from the mooring at 117.895°E are estimated by assuming the continental slope is a vertical wall (a good assumption for the shallow diurnal motions); then, the separate fluxes are estimated from the ratio of the total energy to the flux with knowledge of the distance between the mooring and the wall.

Integrated dissipation on the slope and shelf is computed from the available observations by simply integrating in depth and multiplication by the areas indicated in Figure 3c, which assumes that the observed locations are representative. Because the validity of this assumption is not known, the estimates are uncertain by at least a factor of two.

Model uncertainty

The skill of the models is evaluated by first comparing energy flux estimates point-by-point with observations, and then comparing integrated conversion and energy flux between the different models. Far-field model and observed flux magnitude are generally within a factor of two of each other, with flux direction agreeing to about 30^{o} (Figure E1). Modeled D2 fluxes are about twice observed values at the northern stations (N1, N2, LS02; see ref. 15 for station locations), suggesting the possibility of a high bias in the model in that region. However, glider and far-field model values just west of these stations are in agreement[53], suggesting instead that the poorer agreement at these stations may be due to the extremely steep slopes at those locations.

Additional uncertainty arises from the differences between the models, which is also approximately a factor of two in energy (Table E1). Specifically, near-field conversion (defined below) and radiated flux in the near field model exceed those in the far field and Kuroshio models by nearly a factor of two, likely because of the near field model's higher resolution. All three models have very similar spatial patterns, consistent with those inferred from observations (Figure 2a; refs. 15, 17). Taking into account the factor-of-two scatter between the observations and the far-field model, and this factor-of-two difference between the different models, we choose to use the far-field model in the energy budget calculation, and estimate an overall factor-of-two uncertainty in all model flux and conversion estimates.

Data

Data for each figure are included in spreadsheet form in the Source Data section.

Methods References

31. Egbert, G. & Erofeeva, S. Efficient inverse modeling of barotropic ocean tides. *J. Atmos. Ocean. Tech.* 19, 183–204 (2002).

32. Smith, W. H. F. & Sandwell, D. T. Global sea floor topography from satellite altimetry and ship depth soundings. *Science* 277, 1957–1962 (1997).

33. Teague, W. J., Carron, M. J. & Hogan, P. J. A comparison between the generalized Digital Environmental Model and Levitus climatologies. *J. Geophys. Res.* 95, 7167 – 7183 (1990).

34. R. Hallberg and P. Rhines. Buoyancy-driven circulation in an ocean basin with isopycnals intersecting the sloping boundary. J. Phys. Oceanogr., 26:914–940, 1996.

35. H. L. Simmons, M.-H. Chang, Y.-T. Chang, S.-Y. Chao, O. Fringer, C.R. Jackson, and D.S. Ko. Modeling and prediction of internal waves in the South China Sea. Oceanography, 24:88–99, 2011.

36. John Marshall, Alistair Adcroft, Chris Hill, Lev Perelman, and Curt Heisey. A finite-volume, incompressible Navier Stokes model for studies of the ocean on parallel computers. J. Geophys. Res., 102(C3):5753– 5766, 1997.

37. Ko, D. S., Martin, P. J., Rowley, C. D. & Preller, R. H. A real-time coastal ocean prediction experiment for MREA04. *Journal of Marine Systems* 69, 17–28 (2008).

38. Chen, Y.-J., Shan Ko, D. & Shaw, P.-T. The generation and propagation of internal solitary waves in the South China Sea. *Journal of Geophysical Research: Oceans* 118, 6578–6589 (2013).

39. Ma, B. B., Lien, R.-C. & Ko, D. S. The variability of internal tides in the Northern South China Sea. *Journal of oceanography* 69, 619–630 (2013).

40. Ko, D. S., Chao, S.-Y., Huang, P. & Lin, S. F. Anomalous Upwelling in Nan Wan: July 2008. *Terrestrial, Atmospheric & Oceanic Sciences* 20 (2009).

41. Chassignet, E. P. *et al.* The HYCOM (HYbrid Coordinate Ocean Model) data assimilative system. *J. Mar. Syst.* 65, 60–83 (2007).

42. Sherman, J., R. Davis, W. Owens, and J. Valdes. The autonomous underwater glider ‘‘Spray,’’ IEEE J. Oceanic Eng., 26(4), 437–446 (2001).

43. K. Doherty, D. Frye, S. Liberatore, and J. Toole. A moored profiling instrument. J. Atmos. Ocean. Tech., 16:1816–1829, 1999.

44. Li, Q., Farmer, D. M., Duda, T. F. & Ramp, S. Acoustical measurement of nonlinear internal waves using the inverted echo sounder. *J. Atmos. Ocean. Tech.* 26, 2228–2242 (2009).

45. M. C. Gregg. Estimation and geography of diapycnal mixing in the stratified ocean. In J. Imberger, editor, Physical Processes in Lakes and Oceans, volume 54, pages 305–338. American Geophysical Union, Washington, D.C., 1998.

46. Dillon, T. M. Vertical overturns: A comparison of Thorpe and Ozmidov length scales. *J. Geophys. Res.* 87, 9601–9613 (1982).

47. Ferron, B. H., Mercier, H., Speer, K., Gargett, A. & Polzin, K. Mixing in the Romanche Fracture Zone. *J. Phys. Oceanogr.* 28, 1929–1945 (1998).

48. Alford, M. H., Gregg, M. C. & Merrifield, M. A. Structure, propagation and mixing of energetic baroclinic tides in Mamala Bay, Oahu, Hawaii. *J. Phys. Oceanogr.* 36, 997–1018 (2006).

49. Mater, B. D., Schaad, S. M. & Venayagamoorthy, S. K. Relevance of the Thorpe length scale in stably stratified turbulence. *Phys. Fluids,* 25, 076604 (2013).

50. Althaus, A., Kunze, E. & Sanford, T. Internal tide radiation from Mendocino Escarpment. *J. Phys. Oceanogr.* 33, 1510–1527 (2003).

51. Pickering, A. I., Alford, M. H., Rainville, L., Nash, J. D. & Lim, B. Spatial and temporal variability of internal tides in Luzon Strait. *J. Phys. Oceanogr.* submitted (2014).

52. Nash, J. D., Alford, M. H. & Kunze, E. Estimating internal-wave energy fluxes in the ocean. *J. Atmos. Ocean. Tech.* 22, 1551–1570 (2005).

53. Johnston, T. M. S., Rudnick, D. L., Alford, M. H., Pickering, A. I. & Simmons, H. L. Internal tidal energy fluxes in the South China Sea from density and velocity measurements by gliders. *J. Geophys. Res.* 118, 10.1002/jgrc.20311 (2013).

54. Moum, J. N., Klymak, J. M., Nash, J. D., Perlin, A. & Smyth, W. D. Energy transport by nonlinear internal waves. *J. Phys. Oceanogr.* 37, 1968–1988 (2007).

55. Kelly, S. & Nash, J. D. Internal-tide generation and destruction by shoaling internal tides. *Geophys. Res. Lett.* 37 (2010).

56. Klymak, J. M. & Legg, S. M. A simple mixing scheme for models that resolve breaking internal waves. *Ocean Modell.* 33, 224 – 234 (2010).

57. Alford, M. H., Klymak, J. M. & Carter, G. S. Breaking internal lee waves at Kaena Ridge, Hawaii. *Geophys. Res. Lett.* 41, 906–912 (2014). 24

58. Chang, M.-H., Lien, R.-C., Tang, T.-Y., D'Asaro, E. & Yang, Y.-J. Energy flux of nonlinear internal waves in northern South China Sea. *Geophys. Res. Lett.* 33, doi:10.1029/2005GL025196 (2006).

59. St. Laurent, L. C., Simmons, H. L., Tang, T. Y. & Wang, Y. H. Turbulent properties of internal waves in the South China Sea. *Oceanography* 24, 78–87 (2011).

Extended Data Figure and Table Legends

Figure E1. Comparison of observed and model energy flux. (a) Scatter plot of flux magnitude from observations (y-axis) and far-field model (x-axis). Error bars are ±20% for observed values and ±10% for model values (see Methods text). (b) As (a) but for direction; error bars are ±30^{o}. See Supplementary Information for station locations.

Table E1. Conversion and flux integrated over the region 19-21.5, 120-122.5.

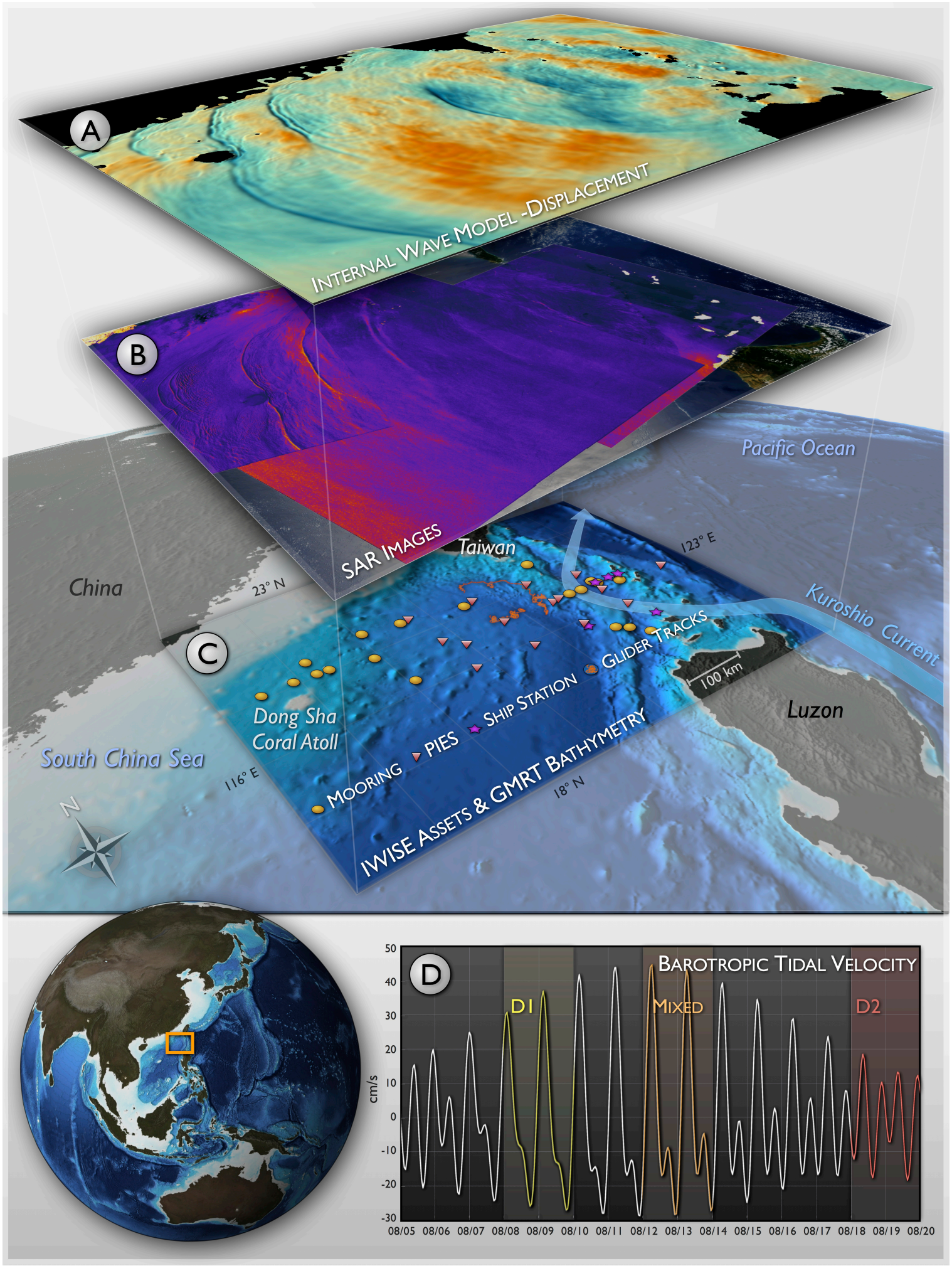
A
INTERNAL WAVE MODEL -DISPLACEMENT
B
SAR IMAGES
Pacific Ocean
Taiwan
123° E
China
23° N
Kuroshio Current
C
GLIDER TRACKS
100 km
Luzon
Dong Sha
Coral Atoll
SHIP STATION
PIES
MOORING
South China Sea
116° E
18° N
IWISE ASSETS & GMRT BATHYMETRY
N
D
BAROTROPIC TIDAL VELOCITY
D1
MIXED
D2
cm/s
50
40
30
20
10
0
-10
-20
-30
08/05 08/06 08/07 08/08 08/09 08/10 08/11 08/12 08/13 08/14 08/15 08/16 08/17 08/18 08/19 08/20

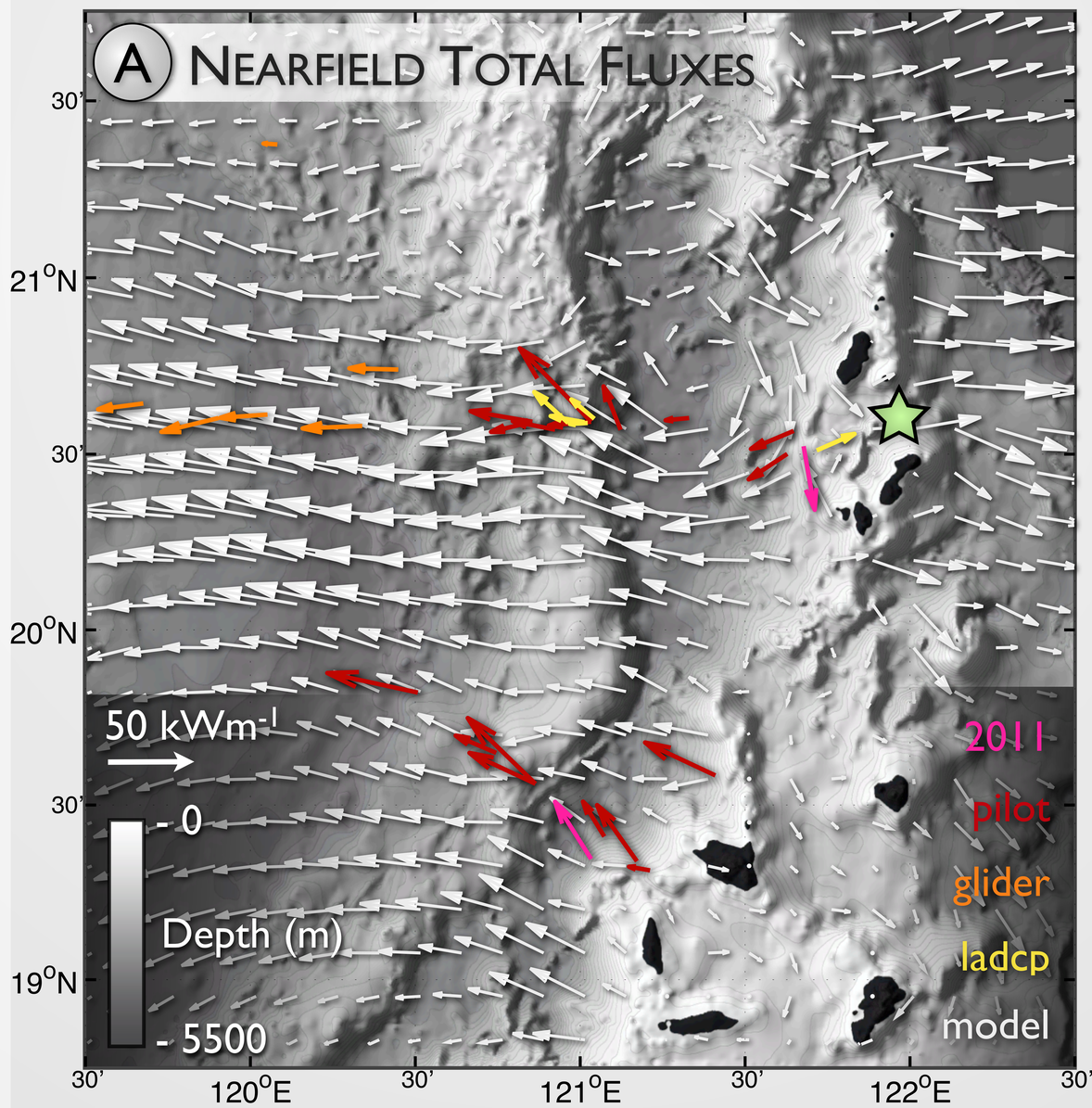
A
Nearfield Total Fluxes
30'
21°N
30'
20°N
30'
19°N
30'
120°E
30'
121°E
30'
122°E
30'
50 kWm-1
0
Depth (m)
5500
2011
pilot
glider
ladcp
model

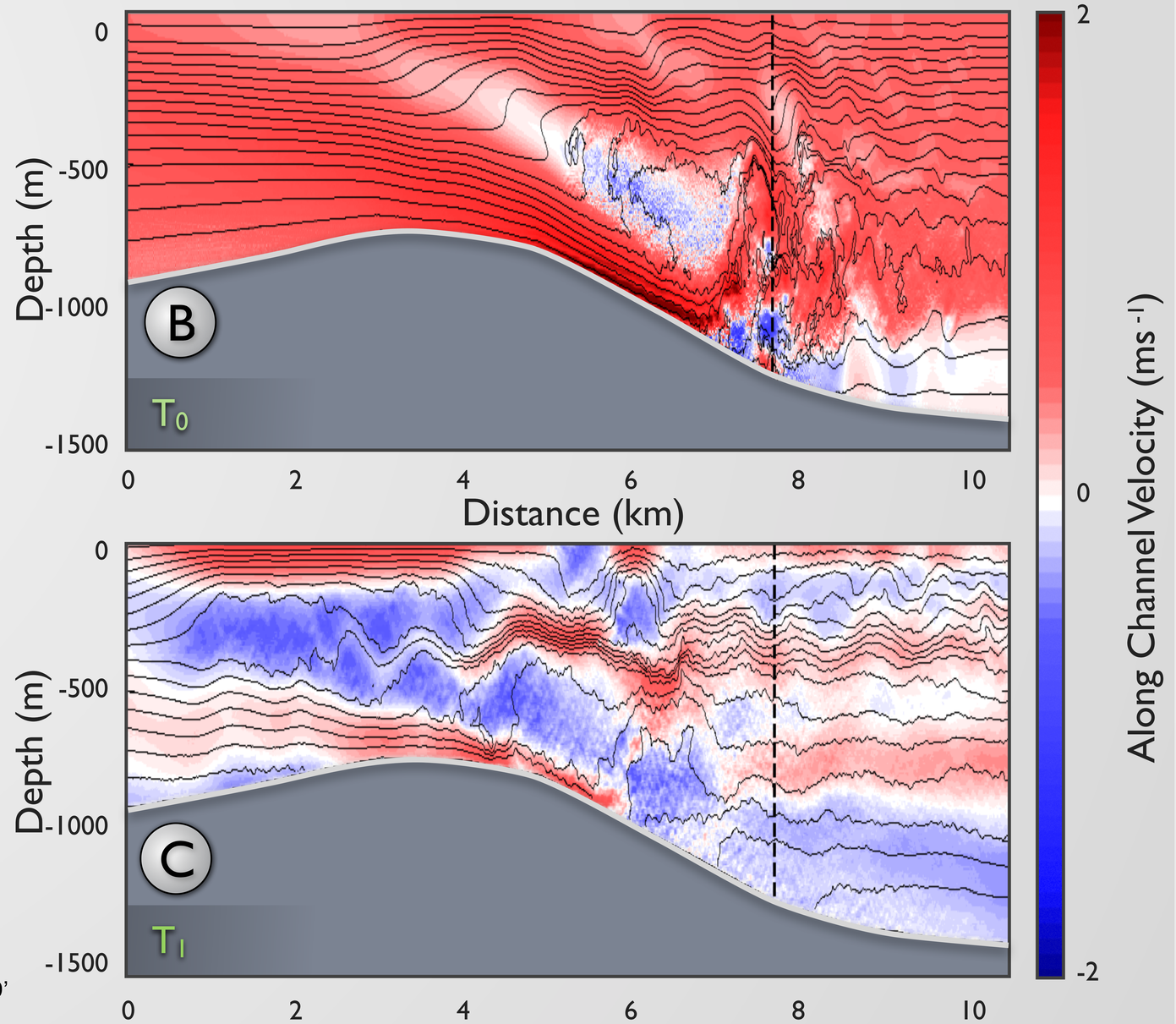
B
T0
C
T1
Depth (m)
0
-500
-1000
-1500
0
2
4
6
8
10
Distance (km)
2
0
-2
Along Channel Velocity (ms-1)

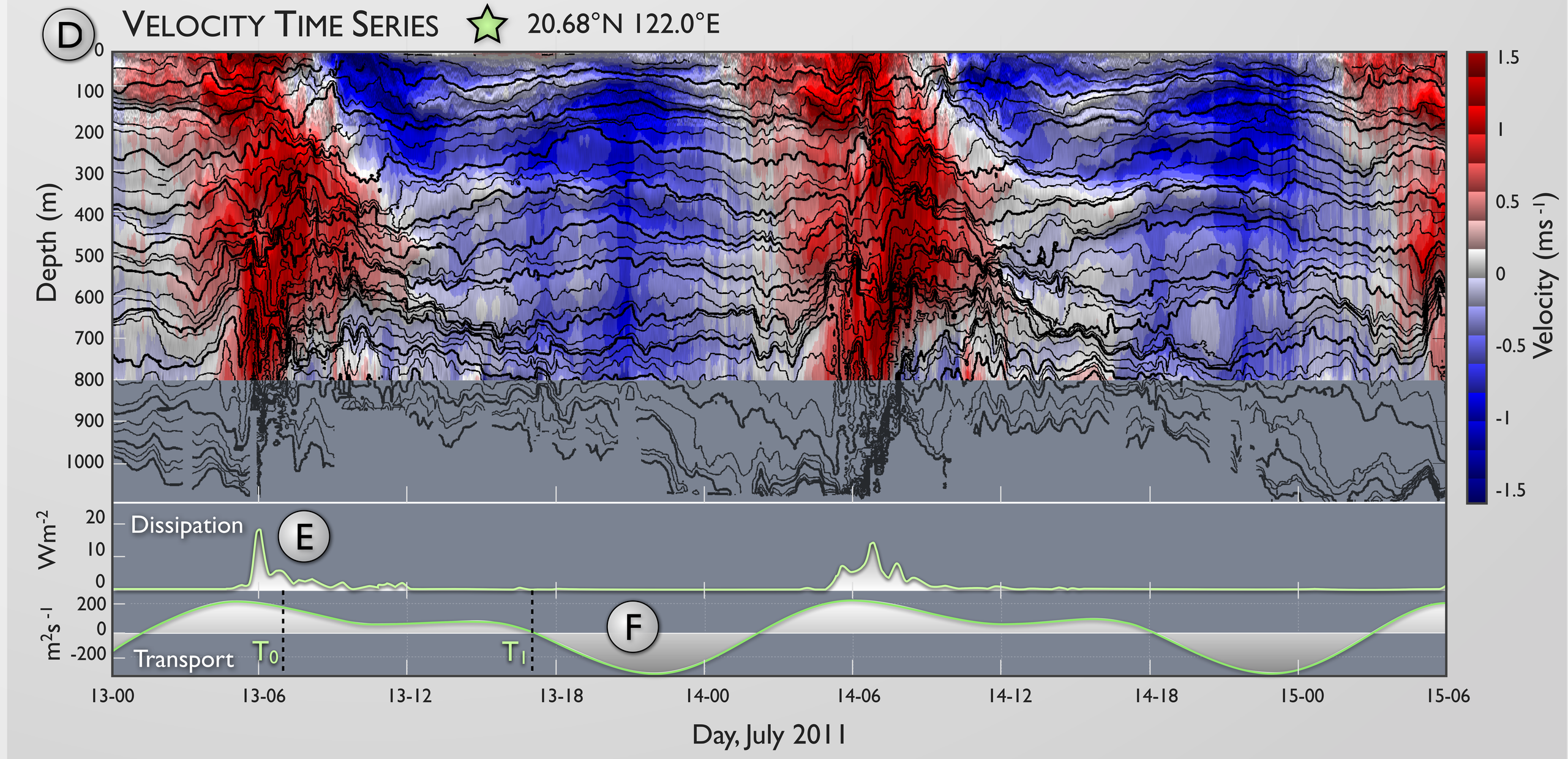
D
Velocity Time Series
20.68°N 122.0°E
Depth (m)
0
100
200
300
400
500
600
700
800
900
1000
1.5
1
0.5
0
-0.5
-1
-1.5
Velocity (ms-1)
Wm-2
20
10
0
Dissipation
E
m2s-1
200
0
-200
Transport
T0
T1
F
13-00
13-06
13-12
13-18
14-00
14-06
14-12
14-18
15-00
15-06
Day, July 2011

23° N

116° E

123° E

18° N

Taiwan

100 km

Luzon

A D2 Fluxes

45.4

kWm^{-1}

0.0

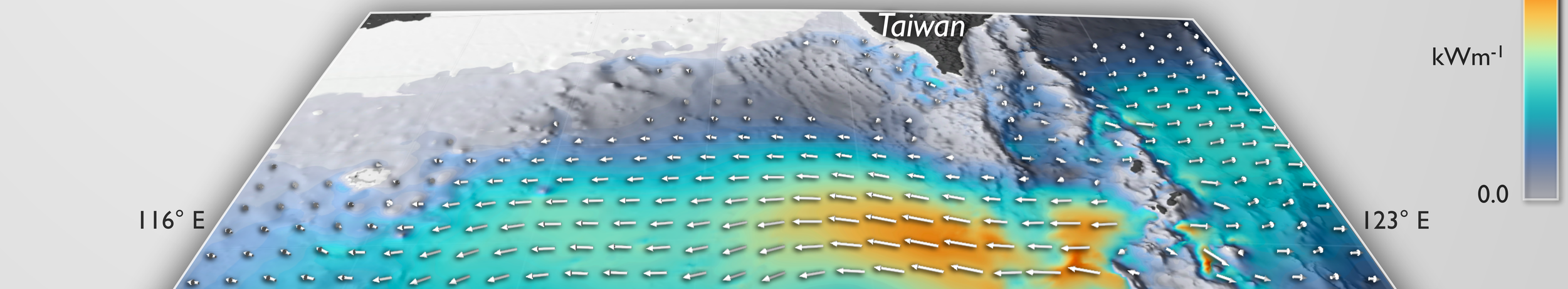

B D1 Fluxes

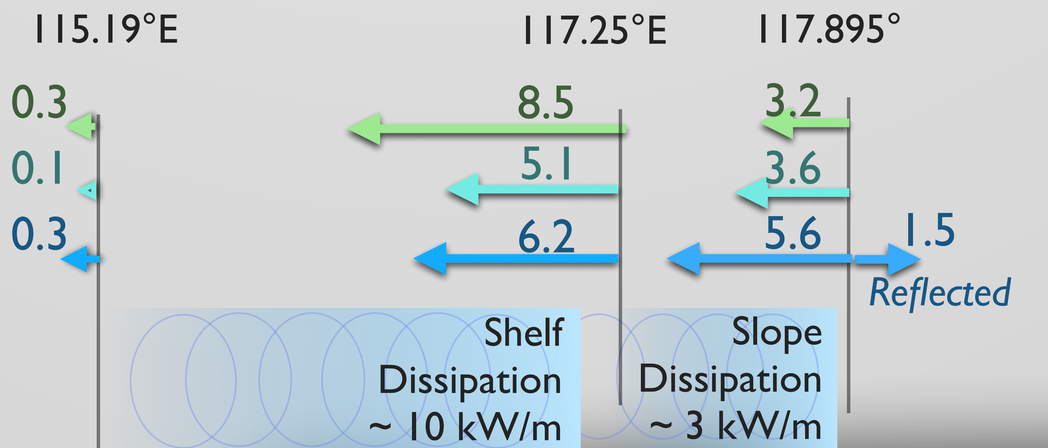

C Integrated Fluxes

NLIW

D2 kWm^{-1}

D1

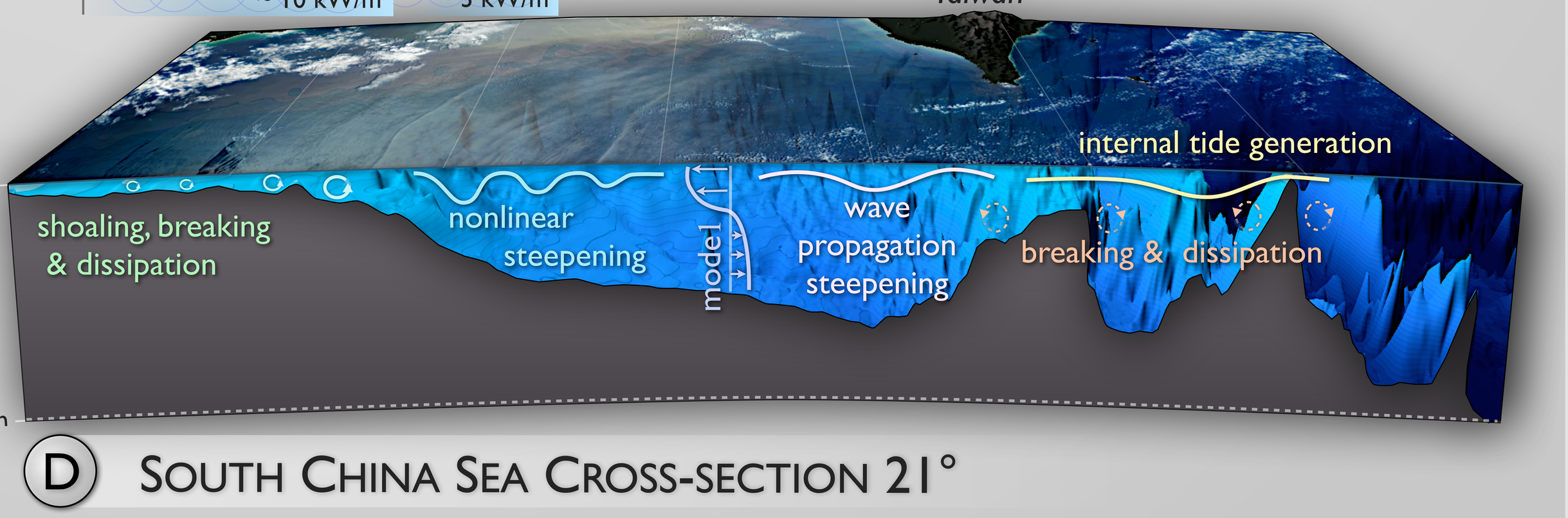

D South China Sea Cross-section 21°

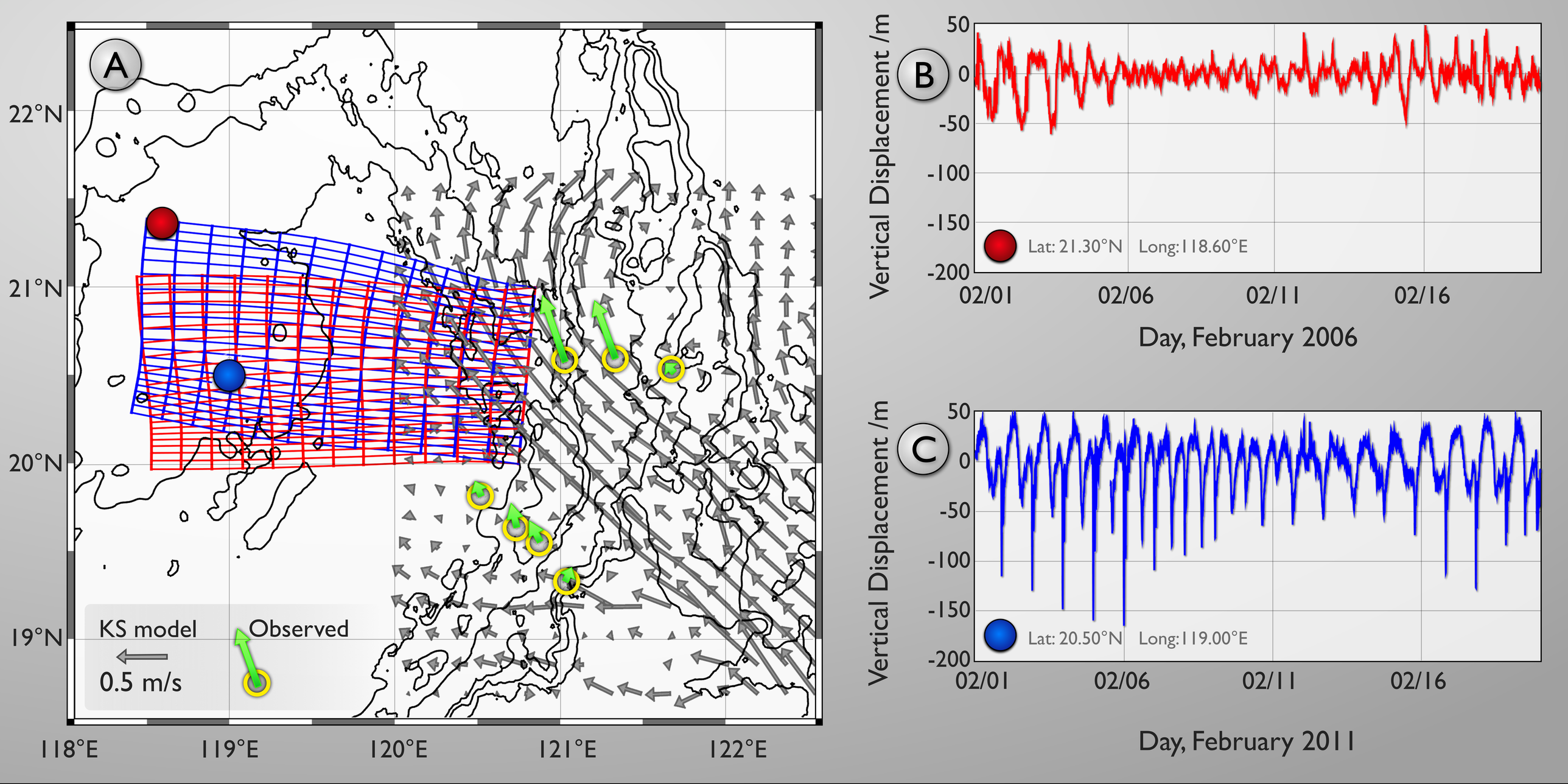
A
22°N
21°N
20°N
19°N
118°E
119°E
120°E
121°E
122°E
KS model
Observed
0.5 m/s
B
Vertical Displacement /m
50
0
-50
-100
-150
-200
Lat: 21.30°N
Long:118.60°E
02/01
02/06
02/11
02/16
Day, February 2006
C
Vertical Displacement /m
50
0
-50
-100
-150
-200
Lat: 20.50°N
Long:119.00°E
02/01
02/06
02/11
02/16
Day, February 2011

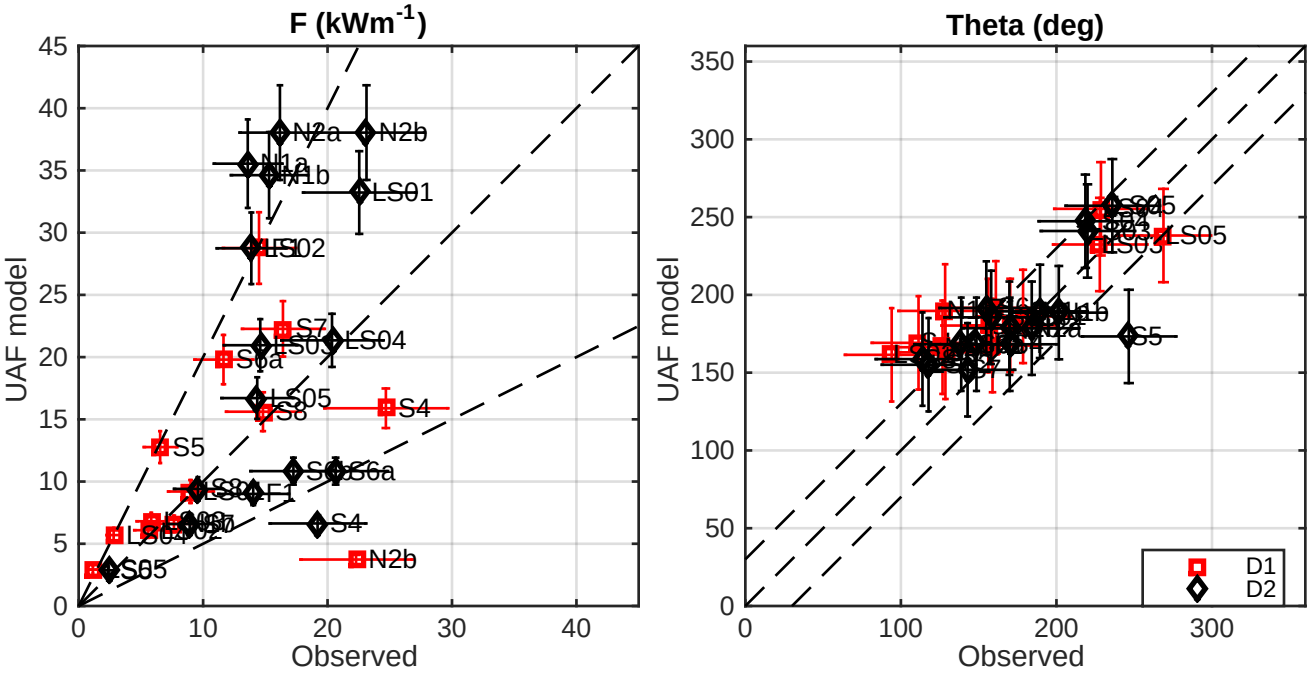
F (kWm-1)
UAF model
Observed
Theta (deg)
UAF model
Observed
D1
D2